

ON THE INITIAL MASS FUNCTION OF POPULATION III STARS

FUMITAKA NAKAMURA

Faculty of Education and Human Sciences, Niigata University, 8050 Ikarashi-2, Niigata 950-2181, Japan

AND

MASAYUKI UMEMURA

Center for Computational Physics, University of Tsukuba, Tsukuba, Ibaraki-ken 305-8577, Japan

submitted to The Astrophysical Journal; Draft version October 24, 2018

ABSTRACT

The collapse and fragmentation of filamentary primordial gas clouds are explored using one-dimensional and two-dimensional hydrodynamical simulations coupled with the nonequilibrium processes of hydrogen molecule formation. The cloud evolution is computed from the initial central density $n_c = 10 - 10^6 \text{ cm}^{-3}$. The simulations show that depending upon the initial density, there are two occasions for the fragmentation of primordial filaments. If a filament has relatively low initial density such as $n_c \lesssim 10^5 \text{ cm}^{-3}$, the radial contraction is slow due to less effective H₂ cooling and appreciably decelerates at densities higher than a critical density, where LTE populations are achieved for the rotational levels of H₂ molecules and the cooling timescale becomes accordingly longer than the free-fall timescale. This filament tends to fragment into dense clumps before the central density reaches 10^{8-9} cm^{-3} , where H₂ cooling by three-body reactions is effective and the fragment mass is more massive than some tens M_\odot . In contrast, if a filament is initially as dense as $n_c \gtrsim 10^5 \text{ cm}^{-3}$, the more effective H₂ cooling with the help of three-body reactions allows the filament to contract up to $n \sim 10^{12} \text{ cm}^{-3}$. After the density reaches $n \sim 10^{12} \text{ cm}^{-3}$, the filament becomes optically thick to H₂ lines and the radial contraction subsequently almost stops. At this final hydrostatic stage, the fragment mass is lowered down to $\approx 1M_\odot$ because of the high density of the filament. The dependence of the fragment mass upon the initial density could be translated into the dependence on the local amplitude of random Gaussian density fields or the epoch of the collapse of a parent cloud. Hence, it is predicted that the initial mass function of Population III stars is likely to be bimodal with peaks of $\approx 10^2 M_\odot$ and $\approx 1M_\odot$, where the relative heights could be a function of the collapse epoch. Implications for the metal enrichment by Population III stars at high redshifts and baryonic dark matter are briefly discussed.

Subject headings: cosmology: theory — galaxies: formation — hydrodynamics — ISM: clouds — stars: formation

1. INTRODUCTION

The existence of a very first generation of objects, namely Population III, has been originally postulated by the presence of a noticeable amount of heavy elements in Population II stars (see, e.g., Carr, Bond, & Arnett 1984 and references therein) and has recently gained increasing importance owing to the discovery of intergalactic metals in the Ly α forest (Cowie et al. 1995; Songaila & Cowie 1996). In those respects, Population III objects need to be such massive stars that they can produce metals at the end of their evolution. Recent theoretical analyses on the evolution of metal-free stars predict that the fate of the massive metal-free stars can be classified as follows (e.g., Heger, Woosley, & Waters 2000; Chiosi 2000; see also Portinari, Chiosi, & Bressan 1998 for the effects of mass loss.): (1) A star with a mass of $m \gtrsim 250M_\odot$ collapses completely to a black hole (BH) without ejecting any heavy elements (Bond, Carr & Arnett 1984). (2) A star of $100M_\odot \lesssim m \lesssim 250M_\odot$ is partly or completely disrupted by electron-positron pair instability. For $m \gtrsim 150M_\odot$, the core completely disrupts, and the whole core involving heavy elements is injected in the intergalactic medium. If it is an extremely energetic event (a hypernova), it might lead to a gamma ray burst (GRB).

(3) A star of $35M_\odot \lesssim m \lesssim 100M_\odot$ probably collapses into a black hole. (4) A star of $10M_\odot \lesssim m \lesssim 35M_\odot$ results in a type II supernova.

Population III stars are related to various issues that are currently the object of considerable attention. The luminous Population III stars could cause the reionization of the universe at redshifts $\gtrsim 5$ (Couchman & Rees 1986; Fukugita & Kawasaki 1994; Ostriker & Gnedin 1996; Gnedin & Ostriker 1997; Haiman & Loeb 1997; Miralda-Escudé & Rees 1998; Gnedin 2000). Alternatively, moderately massive BHs as the end products of massive stars might coagulate into a super-massive BH, evolving to primordial AGNs (Larson 2000). The accreting super-massive BHs may be more responsible for cosmic reionization (Tegmark & Silk 1994; Sasaki & Umemura 1996; Haiman & Loeb 1998; Valageas & Silk 1999). In addition, Population III stars may play an important role in the early evolution of galaxies (e.g., Tegmark, Silk, & Blanchard 1994; Ostriker & Gnedin 1996) or the early formation of massive BHs of $\sim 10^5 M_\odot$ (Umemura, Loeb, & Turner 1993). They may be responsible for the observed abundance patterns of extremely metal-deficient stars (McWilliam et al. 1995; Ryan, Norris, & Beers 1996; Audouze & Silk 1995; Shigeyama & Tsujimoto 1998). Fi-

nally, if a significant number of MACHOs are ancient white dwarfs (Méndez & Minniti 2000), they may stem from low-mass Population III stars (Carr 1994; Larson 1998; Rees 1999). In the light of all of such possible significant consequences, the initial mass function (IMF) of Population III stars is an issue of undoubted importance.

Many authors have studied the collapse of primordial clouds to estimate the masses of Population III stars (e.g., Matsuda, Sato, & Takeda 1969; Yoneyama 1972; Hutchins 1976; Silk 1977, 1983; Carlberg 1981; Palla, Salpeter, & Stahler 1983; Yoshii & Saio 1986; Nishi et al. 1998). These studies have emphasized the importance of radiative cooling by H_2 molecules because the primordial gas is deficient in heavy elements, which are the most efficient coolants in present-day star formation. In the first collapsed objects, baryonic gas is heated to temperatures above 10^3 K during the contraction. This enhances the H_2 formation rate and causes the H_2 abundance to rise from its initial value of $\sim 10^{-6}$ to a quasi-equilibrium value of $10^{-4} \sim 10^{-3}$ (e.g., Palla et al. 1983; Lepp & Shull 1984; Haiman, Thoul & Loeb 1996). Thus, H_2 molecules cool the gas to a temperature of ~ 500 K. As a result, the Jeans mass descends to a stellar mass and Population III stars can form in this way through fragmentation of the first collapsed objects. Although many elaborate analyses have been made, the estimated masses of Population III stars have not been well converged. Several authors have suggested that Population III stars were low mass, whereas others have suggested that they were massive or very massive. This discrepancy seems to come from most studies being restricted to highly simplified models such as homogeneous, pressureless, and/or spherical collapses.

In the bottom-up scenarios like cold dark matter (CDM) models, the first collapsed pregalactic objects should form at redshifts of $z \sim 10 - 10^2$ and have masses of $10^5 \sim 10^8 M_\odot$ (Tegmark et al. 1997). Because of the asymptotic scale-invariance of the CDM density fluctuations, pregalactic clouds with this mass range could undergo a run-away collapse, forming cores of $\sim 10^2 M_\odot$ (Abel et al. 1998; Abel, Norman, & Bryan 2000), or form mini-pancakes, fragmenting into pieces of $10^2 M_\odot - 10^3 M_\odot$ (Bromm, Coppi, & Larson 1999). In these calculations, one of the common features is the formation of a filamentary structure. Filamentary clouds are gravitationally unstable and likely to fragment into dense clumps. Such dense clumps are expected to evolve into Population III stars. The physics of the fragmentation of filamentary primordial clouds has been studied analytically (Uehara et al. 1996) or by a one-dimensional numerical simulation (Nakamura & Umemura 1999, hereafter Paper I). These studies suggest that the minimum mass of Population III stars is of the order of M_\odot . However, the physical processes are still unclear to determine whether Population III stars can be far above M_\odot or be eventually reduced to a few M_\odot . Thus, as a further step following Paper I, we here perform two-dimensional hydrodynamical simulations. Attention is focused on elucidating the physical process of the fragmentation of primordial gas filaments to assess the mass of Population III stars.

In Paper I, we pursued the radial contraction of primordial filaments and showed that the filaments continue to contract quasi-statically, the temperatures staying nearly constant at $T \sim 500$ K. When the cloud becomes opti-

cally thick to the H_2 lines, the radial contraction essentially stops. Applying a linear stability analysis, the fragmentation was expected to take place at that stage and the minimum masses of Population III stars were estimated as a few M_\odot . Thus, Population III stars were anticipated to be low-mass deficient compared to the present-day stars. In this paper, we pursue the fragmentation processes of the filaments by means of two-dimensional axisymmetric simulations. The present model is an improved version of Paper I. The numerical model and method are described in §2. Numerical results are given in §3 and §4. We show that filaments with low initial density can fragment into dense clumps before the cloud becomes optically thick to the H_2 lines. Then, the masses of the clumps could be much more massive than a few M_\odot . However, relatively dense filaments result in clumps of a few M_\odot . Hence, in §5, it is predicted that the initial mass function of Population III stars is likely to be bimodal. In §6, we discuss some implications for the first metal enrichment and baryonic dark matter.

2. MODEL AND NUMERICAL METHODS

2.1. Basic Equations

To pursue the collapse and fragmentation of filamentary primordial clouds, we employ a two-dimensional hydrodynamical scheme. We assume that the system is axisymmetric and that the medium consists of ideal gas. The adiabatic index, γ , is taken to be 5/3 for monatomic gas and 7/5 for diatomic gas. We deal with the following 9 species: e, H, H^+ , H^- , H_2 , H_2^+ , He, He^+ , and He^{++} . The mass fraction of He is taken to be 0.24 of the total mass.

The basic equations are then described as

$$\frac{\partial \rho}{\partial t} + \nabla \cdot (\rho \mathbf{v}) = 0, \quad (1)$$

$$\frac{\partial(\rho \mathbf{v})}{\partial t} + \nabla \cdot (\rho \mathbf{v} \otimes \mathbf{v}) + \nabla P + \rho \nabla \psi = 0, \quad (2)$$

$$\frac{\partial E}{\partial t} + \nabla \cdot [(E + P)\mathbf{v}] + \rho \mathbf{v} \cdot \nabla \psi + \Lambda_{\text{net}} = 0, \quad (3)$$

$$\Delta \psi = 4\pi G \rho, \quad (4)$$

$$\rho = \sum_i \rho_i, \quad (5)$$

$$P = \sum_i P_i = \sum_i n_i k T, \quad (6)$$

$$E = \sum_i \left(\frac{P_i}{\gamma_i - 1} + \frac{1}{2} \rho_i \mathbf{v}^2 \right), \quad (7)$$

where ρ is the mass density, n is the number density, \mathbf{v} is the velocity, P is the gas pressure, ψ is the gravitational potential, E is the energy per unit volume, G is the gravitational constant, and k is the Boltzmann constant. The symbol Λ_{net} denotes the net energy-loss rate per unit volume. The values with subscript i denote those of the i -th species.

The number density of the i -th species, n_i , is obtained by solving the following time-dependent rate equations,

$$\frac{dn_i}{dt} = \sum_{j=1}^9 \sum_{k=1}^9 k_{jk} n_j n_k + \sum_{l=1}^9 \sum_{m=1}^9 \sum_{n=1}^9 k_{lmn} n_l n_m n_n, \quad (8)$$

where the reaction rate coefficients, k_{jk} and k_{lmn} , are given in Table 1. The relative abundances of hydrogen species are given by $x_i \equiv n_i/n$, where $n \equiv n_{\text{H}} + n_{\text{H}^+} + n_{\text{H}^-} + 2n_{\text{H}_2} + 2n_{\text{H}_2^+}$.

We take into account the following thermal processes by H atoms and H₂ molecules: (1) H cooling by recombination, collisional ionization, and collisional excitation (Cen 1992), (2) H₂ line cooling by rotational and vibrational transitions (see below), (3) cooling by H₂ collisional dissociation (Shapiro & Kang 1987), and (4) heating by H₂ formation (Susa, Uehara, & Nishi 1996). In Paper I, for the H₂ formation heating, we only took into account the contributions by two-body reactions (Shapiro & Kang 1987). In this paper, we include the contributions by three-body reactions, which play an important role in temperature evolution after the density reaches 10⁹ cm⁻³ (see §3). Other thermal processes are negligible because the gas temperatures did not exceed 10⁴ K in the models calculated in this paper.

As shown by many authors, H₂ line cooling is most efficient in primordial gas. Therefore, careful evaluation of the H₂ line cooling rate is necessary. We thus compute the H₂ line cooling rate as follows. First, the level populations at the rotational and vibrational excitations are determined by using a recursion formula (Hutchins 1976; Palla et al. 1983). For the collisional deexcitation rates, we consider both H-H₂ and H₂-H₂ collisions using the analytical fits of Hollenbach & McKee (1979) and Galli & Palla (1998). The 21 rotational and 3 vibrational levels are taken into account. Next, a photon escape probability method is applied for each transition (Castor 1970; Goldreich & Kwan 1974). Finally, the line cooling rate is computed as

$$\Lambda_{\text{H}_2\text{line}} = \sum \Lambda_{ij} = \sum n_{l,i} A_{ij} h\nu_{ij} \beta_{ij}, \quad (9)$$

where $n_{l,i}$ is the H₂ level population at level i , A_{ij} is the Einstein A-coefficient, and $h\nu_{ij}$ is the energy difference between levels i and j . The photon escape probability β_{ij} is defined as

$$\beta_{ij} = \frac{1 - \exp(-\tau_{ij})}{\tau_{ij}}, \quad (10)$$

and

$$\tau_{ij}(r, z) = \int_r^{r_{\text{out}}} \alpha_{ij}(r', z) dr' \quad (11)$$

$$= \int_r^{r_{\text{out}}} \frac{h\nu_{ij}}{8\pi\Delta\nu_{ij}} (n_{l,j} B_{ji} - n_{l,i} B_{ij}) dr', \quad (12)$$

where $\tau_{i \rightarrow j}$ is the optical depth at the transition $i \rightarrow j$, r_{out} is the radius of the cloud surface, $\alpha_{i \rightarrow j}$ is the absorption coefficient of the transition $i \rightarrow j$, B_{ij} and B_{ji} are the Einstein B-coefficients, and $\Delta\nu_{ij}(\propto T^{1/2})$ is the thermal Doppler width of the transition line $i \rightarrow j$. Our cooling function almost coincides with that of Galli & Palla (1998) as long as the cloud is optically thin to the H₂ lines. However, once the cloud becomes opaque to the cooling radiation, our cooling rate significantly deviates from that of Galli & Palla (1998).

2.2. Model of Filamentary Primordial Clouds

In bottom-up scenarios such as CDM models, the first collapsed objects at $z \sim 10 - 100$ are expected to have masses of $10^{5-8} M_{\odot}$. In these clouds, the gas is heated above $T > 10^{3-5}$ K by shock. Therefore, just after the shock formation, the cooling timescale is likely to be shorter than the free-fall one. Then, the gas is cooled by the H₂ cooling down to the temperature at which the cooling timescale is comparable to the free-fall one (e.g., Haiman et al. 1996; Yoneyama 1972). The resultant gas temperature is estimated to be $T \simeq 10^{2-3}$ K, depending weakly on the gas density and the H₂ fraction. Recent numerical simulations have shown that such clouds tend to fragment into filaments that collapse toward the major axes (e.g., Bromm et al. 1999; Tsuribe 2000). The collapsing filaments are expected to fragment into denser clumps where Population III stars will form. A model of such a filamentary cloud is described below.

The model of a filamentary cloud is basically the same as that presented in Paper I. We consider an infinitely long cylindrical gas cloud that is collapsing in the radial direction. The initial temperature and relative abundances are assumed to be spatially constant. At the initial state, the relative abundances of H⁻, H₂⁺, He⁺, and He⁺⁺ are set to zero for simplicity. We do not consider the effect of dark matter because after virialization of the parent system, the local density of baryonic gas is likely to become higher than the background dark matter density owing to radiative cooling (e.g., Cen & Ostriker 1992a, 1992b; Umemura 1993). The density is assumed to be uniform along the cylinder axis and its radial distribution is expressed as

$$\rho = \rho_0 \left(1 + \frac{r^2}{R_0^2} \right)^{-2}, \quad (13)$$

where $R_0 = \sqrt{2fkT_0/(\pi G\rho_0\mu)}$ is the effective radius, ρ_0 is the central mass density, T_0 is the initial gas temperature, μ is the mean molecular weight, and f is the ratio of the gravitational force to the pressure force. When $f = 1$, the density distribution coincides with that of an isothermal filament in equilibrium (Stod  kiewicz 1963). In this paper, we restrict the parameter f to $f > 1$ since we are interested in the evolution of collapsing clouds.

The radial infall velocity is given by

$$v_r = -\frac{v_0 r}{R_0 + \sqrt{R_0^2 + r^2}}, \quad (14)$$

which has a qualitatively similar distribution to that of a self-similar solution of a collapsing filament (see Figure 6 of Paper I). Here, v_0 is constant and is set to an initial sound speed (c_s) for all the models calculated in this paper. We also calculated the evolution of the models with different velocity distributions, e.g., $v_r = -v_0 \sin(\pi r/R_{\text{max}})$ and confirmed that the numerical results are not sensitive to the assumed velocity profiles as long as $v_0 \lesssim$ a few $\times c_s$. This is because even if the initial cloud is static, the radial contraction is immediately accelerated owing to the H₂ cooling.

For the above model, the mass per unit length (line mass) is given by

$$l_0 = \int_0^{\infty} 2\pi \rho r dr = \frac{2fkT_0}{\mu G}$$

$$= 1.8 \times 10^3 M_{\odot} \text{pc}^{-1} \left(\frac{f}{2} \right) \left(\frac{T_0}{300 \text{K}} \right). \quad (15)$$

Note that the line mass of the equilibrium ($f = 1$) filament depends only on the temperature. When the filamentary cloud forms through the gravitational fragmentation of a parent sheetlike cloud, its line mass is expected to be nearly twice that of the equilibrium cloud (see §2.2 of Paper I). We thus adopt $f \sim 1.5$ for typical models.

This model is then specified by the five parameters: $n_0 \equiv \rho_0/\mu$, T_0 , f , x_e , and x_{H_2} . The abundances of x_e , x_{H} , and x_{H^+} are determined by the conservation of mass and charge. The initial density of the filament depends sensitively on the properties of the parent cloud such as the mass, collapse redshift, and spin parameter (see the Appendix). Thus, we take a wide range of the initial density, $10 \text{ cm}^{-3} \leq n_0 \leq 10^6 \text{ cm}^{-3}$. Previous numerical simulations (e.g., Haiman, Rees, & Loeb 1996; Abel et al. 1998; Bromm et al. 1999) have shown that the temperatures and H_2 relative abundances reach $T \sim 300 - 500 \text{ K}$ and $x_{\text{H}_2} \sim 10^{-3} - 10^{-4}$, respectively, when the first collapsed objects with masses of $10^{5-8} M_{\odot}$ are virialized. Thus, the initial temperatures and H_2 abundances are set to $T = 300 \sim 500 \text{ K}$ and $x_{\text{H}_2} \sim 10^{-3} - 10^{-4}$, respectively. The electron abundance is set to 5×10^{-5} for all models. As mentioned in Paper I, the numerical results do not depend sensitively upon x_e as far as $x_e \gtrsim 10^{-7}$, because free electrons can quickly recombine to a level of $x_e \lesssim 10^{-7}$ in the course of the collapse.

2.3. Density Fluctuations and Initial Parameters

The initial model of the computation is constructed by imposing linear density fluctuations on the model filament described in the above subsection. The power spectrum of the density fluctuations is assumed to be a power law distribution of $P(k) = Ak^{\nu}$ on a wavenumber space, where k is the wavenumber of the density fluctuation in the z -direction and ν is the power index. The phase of the fluctuations has a random distribution in the range of 0 to 2π . In this paper, the power index ν is taken to be $\nu = -2, -1$, and 0. (Note that $\nu = -1$ provides scale-invariant fluctuations in the present geometry.) The amplitude is specified by $\delta \equiv [P(k)k]^{1/2}$ at $k = 2\pi/R_0$. The simulations were done in the range of $0.1 \geq \delta \geq 0.001$.

Table 2 summarizes the initial parameters of the numerical models calculated in this paper.

2.4. Numerical Methods

The hydrodynamic equations (1) through (7) are solved numerically using a second-order upwind scheme based on the method by Nobuta & Hanawa (1999). See Nobuta & Hanawa (1999) for more details and the test of the code. The rate equations (8) are solved numerically with the LSODAR (Livermore Solver for Ordinary Differential equations with Automatic method switching for stiff and non-stiff problems) coded by L. Petzold and A. Hindmarsh.

The computations are performed on a cylindrical domain ($0 \leq r \leq R_{\text{max}}$ and $0 \leq z \leq Z_{\text{max}}$) with a fixed boundary condition at $r = R_{\text{max}}$ and periodic boundary conditions at $z = 0$ and Z_{max} , where R_{max} and Z_{max} are the maximum r - and z -coordinates on the computational domain, respectively. Uniform grids are employed for all

runs. In all the models we take R_{max} to be more than three times the effective radius R_0 . The effect of the fixed boundary is very small. This is because the density is much lower near the outer boundary ($r \sim R_{\text{max}}$) than at the center, i.e., $\rho \lesssim 10^{-3} \rho_c$ for all runs. In fact, we have calculated the cases with larger R_{max} and have confirmed that the numerical results are not affected.

3. RADIAL CONTRACTION OF FILAMENTARY CLOUDS

Before examining the fragmentation processes of filamentary clouds, we pursue the evolution of the filamentary clouds with no density fluctuations, i.e., their radial contraction. These calculations are the extension of Paper I. (In Paper I, we explored the evolution of the filaments in the initial density range of $10^2 \text{ cm}^{-3} \leq n_0 \leq 10^4 \text{ cm}^{-3}$. In this paper, we extend the initial density range to $10 \text{ cm}^{-3} \leq n_0 \leq 10^6 \text{ cm}^{-3}$.) In the following we focus on the evolution of physical quantities on the z -axis. See Paper I for more details, e.g., the radial distributions of the physical quantities. As shown below, the evolution of the filaments can be classified into two types, depending mainly on the initial density.

3.1. A Low-Density Filament: A Quasi-Statically Contracting Filament (Model A1a)

As a typical example of low-density filaments, we show the evolution of model A1a which has the initial parameters of $n_0 = 10 \text{ cm}^{-3}$, $T_0 = 400 \text{ K}$, and $f = 1.5$. The electron and H_2 number fractions are initially set to 5×10^{-5} and 10^{-4} , respectively. Figure 1a shows the evolution of the temperature and the H_2 number fraction as a function of the central density. The central density monotonously increases with time. Therefore, the abscissa corresponds to the evolution time. For comparison, we pursued the evolution of model A1a in which the three-body reactions are not taken into account. The evolutional paths are shown by dotted lines in Figure 1.

Figure 1b shows the evolution of three characteristic timescales as a function of the central density. The solid, dashed, and dashed-dotted lines denote the contraction time, the cooling time, and the fragmentation time, respectively. The dotted lines denote the evolution of the temperature and contraction time for the model without the three-body reactions. The contraction and cooling times are defined as $t_{\text{dyn}} \equiv \rho/\dot{\rho}$ and $t_{\text{cool}} \equiv 3nkT/(2\Lambda_{\text{net}})$, respectively. The fragmentation time is defined to be the inverse of the growth rate of the fastest-growing linear perturbation, $t_{\text{frag}} \equiv 2.07/\sqrt{2\pi G \rho_c}$ (eq. [38] of Nakamura, Hanawa, & Nakano 1993). It should be noted that a filament does not undergo fragmentation in one-dimensional calculations, therefore t_{frag} should be regarded as a measure of the free-fall time.

During the contraction, the temperature stays nearly constant at $T \sim 300 - 500 \text{ K}$ because of the H_2 line cooling. The H_2 number fraction also stays nearly constant at $x_{\text{H}_2} = 10^{-4} \sim 10^{-3}$ until the density reaches $n_c \sim 10^8 \text{ cm}^{-3}$. After that, the three-body reactions for the H_2 formation become dominant. Accordingly, the H_2 number fraction steeply rises around $n_c \sim 10^8 \text{ cm}^{-3}$ and almost all the hydrogen atoms become into H_2 molecules by the stage at which the density reaches $n_c \sim 10^{11} \text{ cm}^{-3}$. In contrast, for the model without the three-body reactions, the H_2 number fraction stays nearly constant at

$x_{\text{H}_2} = 10^{-4} \sim 10^{-3}$ and the contraction stops at the stage at which the density reaches $n_c \sim 10^9 \text{ cm}^{-3}$.

The heating rate by H_2 formation also becomes appreciable when the three-body reactions become dominant. Therefore, the temperature rises slowly after the density reaches $n_c \sim 10^9 \text{ cm}^{-3}$. Note that the H_2 line cooling rate is always the most efficient during the contraction.

During the contraction, the contraction time nearly coincides with the cooling time until the central density reaches $2 \times 10^{11} \text{ cm}^{-3}$. This indicates that the cloud collapses in a cooling time. After the central density reaches 10^4 cm^{-3} , the contraction proceeds quasi-statically because the contraction time becomes longer than the fragmentation time. In other words, if there are fluctuations, the cloud is expected to become unstable to fragmentation after the density reaches 10^4 cm^{-3} . Such evolution is explained as follows. A density of 10^4 cm^{-3} is almost comparable to a critical density of H_2 , $n_{\text{cr}} \sim 10^{3-4} \text{ cm}^{-3}$, beyond which LTE populations are achieved for the rotational levels of hydrogen molecules. If the density is less than n_{cr} , then the H_2 line cooling rate is nearly proportional to the square of the density, $\Lambda \propto n^2$, and the cooling time is thus inversely proportional to the density, $t_{\text{cool}} \propto n^{-1}$. On the other hand, if the density is greater than n_{cr} , then the H_2 line cooling rate is nearly proportional to the density, $\Lambda \propto n$ and accordingly the cooling time is independent of the density. Therefore, after the density reaches n_{cr} , the cooling time becomes longer than the fragmentation time ($t_{\text{frag}} \propto n^{-1/2}$) when the temperature is nearly constant. (In fact, the cooling time is almost constant during $10^4 \text{ cm}^{-3} \lesssim n_0 \lesssim 10^7 \text{ cm}^{-3}$.) After the central density reaches 10^8 cm^{-3} , the H_2 abundance steeply increases due to the three-body reactions and the radial contraction thus accelerates again owing to the enhanced H_2 line cooling. (In contrast, for the model without three-body reactions, the radial contraction stops when the central density reaches $\sim 10^9 \text{ cm}^{-3}$ because of less effective H_2 cooling.) When the central density reaches $10^{11-12} \text{ cm}^{-3}$, the cloud becomes optically thick to almost all the H_2 lines which significantly contribute to the total cooling rate. Consequently, the contraction essentially stops at that stage.

Such evolution is also related to the dynamical stability of self-gravitating clouds. Assuming the polytropic relation of the equation of state ($P \propto \rho^\gamma$), a hydrostatic cylindrical cloud is stable to radial contraction when $\gamma > \gamma_{\text{cr}} = 1$. In the present model, the temperature is nearly constant during the contraction. In other words, the cloud is in a marginally stable state. Thus, once the H_2 line cooling becomes less effective, the radial contraction easily stops. This is essentially different from that of a spherical cloud. A spherical polytropic gas cloud can continue to collapse as long as $\gamma < \gamma_{\text{cr}} = 4/3$ even if the cooling rate becomes less effective (see §4.1 and Omukai & Nishi 1998).

3.2. A Dense Filament: A Dynamically Collapsing Filament (Model C6a)

As a typical example of dense filaments, we show the evolution of model C6a which has the initial parameters of $n_0 = 10^6 \text{ cm}^{-3}$, $T_0 = 400 \text{ K}$, and $f = 4$. The electron and H_2 number fractions are initially set to 5×10^{-5} and 10^{-4} , respectively. Figures 2a and 2b are the same

as those of Figures 1a and 1b, respectively, but for model C6a.

The evolution is qualitatively similar to that of model A1a, although the temperatures are about two times higher during the contraction. Since the H_2 formation rates by the three-body reactions are inversely proportional to the temperature, the three-body reactions become more effective at the later stages than for model A1a ($n \gtrsim 10^9 \text{ cm}^{-3}$). The contraction time does not become longer than the fragmentation time until the cloud becomes optically thick to the H_2 lines ($n_c \sim 4 \times 10^{12} \text{ cm}^{-3}$). In other words, the contraction proceeds dynamically. This is due to the effective cooling by the three-body reactions. Therefore, the fragmentation is not expected to take place until the cloud becomes optically thick to the H_2 lines ($n_c \sim 10^{12-13} \text{ cm}^{-3}$). Note that, in the model without the three-body reactions, the contraction time becomes longer than the fragmentation time after the central density reaches $\sim 10^{10} \text{ cm}^{-3}$, and the contraction stops when the central density reaches $\sim 10^{11} \text{ cm}^{-3}$, i.e., before the cloud becomes optically thick to the H_2 lines.

3.3. Summary of One-Dimensional Simulations

We pursued the evolution for the other model parameters tabulated in Table 2. We found that the evolution of all the models falls into either of the two types described above, depending mainly on the initial density. When the initial density is lower than $n_0 \lesssim 10^5 \text{ cm}^{-3}$, the contraction time becomes longer than the fragmentation time before the three-body reactions become effective ($n \sim 10^{8-9} \text{ cm}^{-3}$). However, the contraction time does not exceed the fragmentation time until the density becomes greater than n_{cr} , beyond which LTE populations are achieved for the rotational levels of H_2 molecules. On the other hand, when the initial density is greater than $n_0 \gtrsim 10^5 \text{ cm}^{-3}$ and $f \gtrsim 3$, the contraction proceeds dynamically until the cloud becomes optically thick to the H_2 lines ($n_c \sim 10^{12} \text{ cm}^{-3}$). For all the models, the radial contraction essentially stops at the stage at which the cloud becomes optically thick to the H_2 lines which significantly contribute to the total cooling rate.

From the numerical results of the one-dimensional simulations, the filament is likely to fragment into pieces during the stages at which the central density is greater than $\sim 10^4 \text{ cm}^{-3}$ ($\gtrsim n_{\text{cr}}$) and is less than $\sim 10^{12} \text{ cm}^{-3}$ because the radial contraction is appreciably decelerated. When the filament has an initial density lower than 10^5 cm^{-3} , the fragmentation is expected to take place by the stages at which the three-body reactions become effective. On the other hand, when the filament has an initial density greater than 10^5 cm^{-3} , the fragmentation is expected to take place at the stages at which the cloud becomes optically thick to the H_2 lines ($n_c \sim 10^{12} \text{ cm}^{-3}$).

In the next section, we pursue the fragmentation processes with two-dimensional simulations and evaluate the masses of the fragments.

4. FRAGMENTATION OF FILAMENTARY CLOUDS

In this section, to estimate the masses of the fragments, we explore the evolution of collapsing filamentary clouds with density fluctuations by means of two-dimensional simulations.

As shown below, for several models (particularly for models with a large f), radial contraction proceeds to a great degree before the density fluctuations grow nonlinearly. The spatial resolution thus becomes poor before the cloud fragments into smaller clumps. To resolve the fragmentation, we refine grids according to the following procedure: (1) First, in the linear stage of density fluctuations, the cloud evolution for a model is pursued parallel by a one-dimensional calculation without density fluctuations and by a two-dimensional calculation with density fluctuations. The grid spacings used in a one-dimensional calculation are taken to be ten times finer than those of a two-dimensional calculation. The one-dimensional calculation monitors the radial density profiles fairly accurately, while the two-dimensional calculation traces the growth of density fluctuations in the linear stage. (2) When the mean density in the z -axis reaches a reference density ρ_{ref} , which ensures the linear stage (typically $\rho_{\text{ref}} = 10^{3-4} \rho_0$), the density fluctuations in the two-dimensional calculation are Fourier-transformed to give the power spectrum of the fluctuations. (3) Then, the grids in the two-dimensional calculation are refined in the region of $0 \leq r \leq 0.1 R_{\text{max}}$ and $0 \leq z \leq 0.1 Z_{\text{max}}$ and the radial density profiles by the one-dimensional calculation are mapped upon the refined grids. (4) Finally, the Fourier-transformed density fluctuations obtained above are added on the refined two-dimensional grids. Then, the evolution of that model is pursued on the new computational domain. The number of grids is 1024^2 for usual cases and 2048^2 for high-resolution cases.

4.1. A Low-Density Filament (Model A4a)

In this subsection, we show the evolution of model A4a as a typical example of less dense filaments. Figure 3 shows the cross-sections of the cloud at four different stages. This model has the initial parameters of $n_0 = 10^4 \text{ cm}^{-3}$, $T_0 = 400 \text{ K}$, and $f = 1.5$. At the initial state, scale-invariant density fluctuations ($\nu = -1$) with an amplitude of $\delta\rho/\rho = 0.1$ were added. The grid number was set to 2048^2 .

At the early stages, the density fluctuations do not grow appreciably in time because the contraction time is shorter than the fragmentation time [panel (b) of Fig. 3]. When the mean density in the z -axis exceeds $\sim 7 \times 10^6 \text{ cm}^{-3}$, the contraction time becomes longer than the fragmentation time and the density fluctuations begin to grow nonlinearly. As a result, the filamentary cloud fragments into denser clumps by the stages at which the mean density in the z -axis reaches $4 \times 10^7 \text{ cm}^{-3}$ [panels (c) and (d) of Fig. 3]. The masses of the clumps are estimated to be $\sim 250 M_\odot$. The mean separation of the clumps is nearly equal to 0.24 pc which is comparable to the wavelength of the fastest-growing perturbation at the stage at which the mean density in the z -axis reaches 10^7 cm^{-3} .

To see the structures of the clumps more quantitatively, we show the density and temperature distributions in the z -axis in Figure 4. At the early stages, the temperature stays nearly constant at $T \sim 500 \text{ K}$. After the mean density in the z -axis reaches 10^7 cm^{-3} , the density fluctuations grow nonlinearly, and dense prolate clumps form. As the collapse proceeds, the central region of the clump becomes spherical. In the clumps, the contraction is accelerated, and the temperature rises slowly. This acceleration

is related to the dynamical stability of self-gravitating clouds. A cylindrical polytropic ($P \propto \rho^\gamma$) cloud is stable to radial contraction when $\gamma \gtrsim \gamma_{\text{cr}} = 1$. Therefore, the primordial filament collapses quasi-statically because the effective γ is slightly greater than γ_{cr} (see Fig. 1). On the other hand, for a spherical cloud, the critical value of γ is equal to $\gamma_{\text{cr}} = 4/3$. Accordingly, once the fragmentation takes place, the clumps become unstable to dynamical contraction, resulting in a temperature rise. Such evolution is similar to that of the spherical collapse of primordial clouds (e.g., Omukai et al. 1998; Omukai & Nishi 1998).

The evolutions of other models with $n_0 \lesssim 10^{5-6} \text{ cm}^{-3}$ or $f \lesssim 2$ are qualitatively similar to that of this model (e.g., models A1a – A6a, B1a – B6a, C1a – C3a). The fragmentation can take place before the stages at which the three-body reactions become efficient and the radial contraction is reaccelerated.

4.2. A Dense Filament (Model C6a)

In this subsection, we show the evolution of model C6a as a typical example of dense filaments. Figure 5 shows the density and temperature distributions in the z -axis at three different stages. This model has the initial parameters of $n_0 = 10^6 \text{ cm}^{-3}$, $T_0 = 400 \text{ K}$, and $f = 4$. At the initial state, scale-invariant density fluctuations ($\nu = -1$) with an amplitude of $\delta\rho/\rho = 0.1$ were added. As expected from the numerical results of the one-dimensional simulations, the radial contraction proceeds dynamically until the mean density in the z -axis reaches $4 \times 10^{12} \text{ cm}^{-3}$. When the mean density in the z -axis exceeds $4 \times 10^{12} \text{ cm}^{-3}$, the cloud becomes optically thick to the H_2 lines, and the density fluctuations then begin to grow nonlinearly. In this way, the cloud fragments into clumps. The fragment mass is reduced down to $1 - 2 M_\odot$ owing to the high density of the filament.

The evolutions of other models with $n_0 \gtrsim 10^{5-6} \text{ cm}^{-3}$ and $f \gtrsim 2$ are similar to that of this model (e.g., models C4a – C6a). In those models, the fragment masses take their minimum values of $1 - 2 M_\odot$ because the radial contraction proceeds dynamically until the stages at which the H_2 lines become opaque.

4.3. Typical Masses of the Fragments

Figure 6 shows the distribution of the averaged fragment mass derived from the two-dimensional simulations for the models with $\nu = -1$ and $\delta\rho/\rho = 0.1$. The abscissa and ordinate denote the initial central density and the parameter f , respectively. Since for all the models calculated in Figure 6, the initial temperatures are taken to be constant at $T_0 = 400 \text{ K}$, the ordinate specifies the initial line mass. The solid lines denote the contours of the averaged fragment mass. As discussed in the Appendix, the primordial filaments are expected to form by cosmological pancake collapse and fragmentation. For comparison, the line masses of such filaments with $l = l_{\text{eq}}$, $l = 1.5 l_{\text{eq}}$, and $l = 2 l_{\text{eq}}$ are shown by dashed lines in Figure 6 (see eq.[15]). Here, l_{eq} is the line mass of the filament in hydrostatic equilibrium and is determined by the gas temperatures at which the cooling time balances with the fragmentation time of the pancaking disk, where the fragmentation time is defined as the inverse of the growth rate of the fastest-growing linear perturbation (Larson 1985).

The averaged fragment mass depends on the initial parameters. For larger f and/or higher initial density, the fragment mass is lower. As expected from the one-dimensional simulations, the fragmentation takes place during the stages at which $10^4 \text{ cm}^{-3} \lesssim n_c \lesssim 10^{12} \text{ cm}^{-3}$ because the radial contraction proceeds quasi-statically. Then, the maximum and minimum masses are estimated as $10^3 M_\odot$ and $1 \sim 2 M_\odot$, respectively. It is worth noting that these two masses are related to the microphysics of H₂ molecules. The former corresponds to the Jeans mass at the stage at which the density reaches the critical density of H₂ molecules, while the latter corresponds to the Jeans mass at the stage at which the cloud becomes opaque to the H₂ lines.

There is a steep boundary in the fragment mass at $n_0 \sim 10^{5-6} \text{ cm}^{-3}$ and $f \gtrsim 3$. For the models with $n_0 \gtrsim 10^5 \text{ cm}^{-3}$, the fragment masses take their minimums at $1 \sim 2 M_\odot$. On the other hand, for the models with $n_0 \lesssim 10^5 \text{ cm}^{-3}$, they are greater than $\sim 10^2 M_\odot$. This sensitivity in the fragment mass comes from the rapid increase in H₂ abundance due to the three-body reactions. As shown in Figure 1, when the three-body reactions become effective ($n \gtrsim 10^8 \text{ cm}^{-3}$), the radial contraction accelerates again because of the enhanced H₂ line cooling. For models with a smaller initial density ($n_0 \lesssim 10^5 \text{ cm}^{-3}$), linear density fluctuations can grow nonlinearly before the three-body reactions become dominant at $n \lesssim 10^{8-9} \text{ cm}^{-3}$. On the other hand, for models with a denser initial density ($n_0 \gtrsim 10^{5-6} \text{ cm}^{-3}$), the contraction time does not exceed the fragmentation time until the cloud becomes optically thick to the H₂ lines, $n \sim 10^{12} \text{ cm}^{-3}$.

Although the fragment mass also depends on the initial temperature, the effect of the initial temperature is identical to that of parameter f . This is because changing T_0 and/or f corresponds to the change of the line mass (see equation [15]). During the contraction, the cloud temperature is determined by the balance between the heating and cooling rates. In our model, the main heating source is the compressional heating by gravitational contraction, while the main cooling source is the H₂ line transitions. Even if we take higher or lower initial temperature, the cloud temperature settles immediately to an equilibrium value at which the heating rate is equal to the cooling rate. Furthermore, the equilibrium temperature depends only weakly on density ($T_{\text{eq}} \sim 300 - 800 \text{ K}$ for $n_0 = 10 - 10^6 \text{ cm}^{-3}$). Therefore, the ordinate of Figure 6 can be replaced by T_0 if a constant f is adopted.

The fragment mass depends on the amplitude and power index of the density fluctuations. In Figure 7, the results with $\delta = 0.01$ are shown. This figure shows that the dependence on the fluctuation amplitude is quite weak and that the fragment mass is not basically altered. Changing power index ν leads to a change of amplitude for the most unstable mode. It is found that the fragment mass is insensitive to the choice of ν in a range of $-2 \leq \nu \leq 0$.

When the initial H₂ abundance is as high as 10^{-3} , the fragment mass is reduced by a few tens % because of the lower temperatures although the minimum values of the fragment mass do not change.

5. IMPLICATIONS FOR THE IMF OF POPULATION III STARS

As shown in the previous section, the primordial filaments fragment into dense clumps whose masses are in the range of $1M_\odot \lesssim M \lesssim 10^3 M_\odot$. The masses of the clumps depend on the initial model parameters, particularly the initial density. The initial densities of the filaments are related to the initial conditions of the parent clouds. In the Appendix, based on a CDM cosmology, we considered the formation processes of the filaments and estimated plausible initial conditions. From eq. (A4) of the Appendix, the initial densities of the filaments are estimated as $10^3 \text{ cm}^{-3} \lesssim n_0 \lesssim 10^7 \text{ cm}^{-3}$ for 1σ density fluctuations with masses of $M \simeq 10^{6-8} M_\odot$ ($10^4 \text{ cm}^{-3} \lesssim n_0 \lesssim 10^8 \text{ cm}^{-3}$ for 3σ density fluctuations). Then, the clump masses are evaluated as $1M_\odot \lesssim M \lesssim 500M_\odot$ for 1σ density fluctuations ($1M_\odot \lesssim M \lesssim 250M_\odot$ for 3σ density fluctuations). Here, we assumed that the radius of the parent disk ranges from $0.01r_{\text{vir}}$ to $0.1r_{\text{vir}}$, where r_{vir} denotes the virial radius of the parent cloud (see eq. [A1]). The minimum radius corresponds to that of a rotationally supported disk with a spin parameter of $\lambda = 0.05$. The maximum radius is taken from the numerical results by Bromm et al. (1999) who followed the collapse of 3σ 'top-hat' density fluctuations with a mass of $\sim 10^6 M_\odot$. Their numerical simulations indicate that by the epoch of filament formation, the radius of the disk shrinks to $\sim 0.1r_{\text{vir}}$, i.e., before the disk contracts to form a rotationally supported disk, fragmentation takes place.

The dense clumps are expected to be the sites of Population III star formation. Recently, Larson (2000) argues that these clumps are not likely to fragment into many lower-mass objects because their masses are nearly comparable to the Jeans mass at the epoch of fragmentation. Actually, numerical simulations (e.g., Bromm et al. 1999) have shown that the fragmentation of collapsing Jeans-mass clumps is likely to be limited to the formation of binary or small multiple systems.

In the primordial gas, most of the parent clump mass is expected to accrete onto the subclumps that will evolve into Population III stars because metal-free (dust-free) gas is impervious to strong radiation pressure (Omukai 1999, private communication). Thus, the masses of Population III stars are anticipated to become comparable to the masses of the clumps.

As mentioned in the previous section, the dependence of the clump mass on the initial density exhibits a step around $n_0 \sim 10^5 \text{ cm}^{-3}$. Then, the IMF of Population III stars is likely to be low-mass deficient and double-peaked at $m_{\text{p1}} = 1 - 2M_\odot$ and $m_{\text{p2}} = \text{a few} \times 10 - 10^2 M_\odot$. [The first peak is consistent with the estimates by Uehara et al. (1996) and Nakamura & Umemura (1999). The clumps around the second peak have similar masses to those obtained by Abel et al. (1998) and Bromm et al. (1999).] The masses of the clumps probably increase by merging with themselves. The resultant mass spectrum could have two power-law-like components with different peaks of $m_{\text{p1}} \sim 1 - 2M_\odot$ and $m_{\text{p2}} \sim \text{a few} \times 10 - 10^2 M_\odot$. It should be noted that the relative height of the first peak probably descends with time compared to that of the second peak, because the initial densities of the filaments decrease with time. In other words, at higher redshifts or for higher σ density fluctuations, the contribution of the lower-mass component is more significant in the IMF.

6. METAL ENRICHMENT

As discussed in §5, Population III stars are expected to be low-mass deficient compared to present-day stars and their IMF is likely to be bimodal with peaks of $m_{p1} \sim 1 - 2M_{\odot}$ and $m_{p2} \sim \text{a few} \times 10 - 10^2 M_{\odot}$. In Figure 8, we show a schematic IMF of Population III stars.

If each component of the IMF is approximated by a simple power law with a sharp cut-off, then the IMF of Population III stars is expressed as

$$\frac{dN}{d \log m} = \frac{d(N_{\text{low}} + N_{\text{high}})}{d \log m}, \quad (16)$$

where

$$\frac{dN_{\text{low}}}{d \log m} = \begin{cases} Am^{-\alpha} & \text{for } m \geq m_{p1} \\ 0 & \text{for } m < m_{p1} \end{cases} \quad (17)$$

$$\frac{dN_{\text{high}}}{d \log m} = \begin{cases} Bm^{-\beta} & \text{for } m \geq m_{p2} \\ 0 & \text{for } m < m_{p2} \end{cases} \quad (18)$$

where the value of m_{p2} is somewhat arbitrary because it depends on the initial densities of the filaments. The relative heights of two peaks are also related to the power spectrum of the cosmological density fluctuations. If the power indexes of the IMF are greater than unity (α and $\beta > 1$), then the numerical constants A and B are approximated as

$$A \sim (\alpha - 1)\kappa\epsilon M_{\text{total}} m_{p1}^{\alpha-1}, \quad (19)$$

and

$$B \sim (\beta - 1)(1 - \kappa)\epsilon M_{\text{total}} m_{p2}^{\beta-1}, \quad (20)$$

respectively, where M_{total} is the parent cloud mass, ϵ is the star-formation efficiency in the cloud, and κ is the ratio of the mass contained in the lower-mass component to the total stellar mass.

According to recent theoretical studies on the evolution of metal-free stars, the massive metal-free stars with masses of (1) $10M_{\odot} \lesssim M_{\text{star}} \lesssim 35M_{\odot}$ and (2) $150M_{\odot} \lesssim M_{\text{star}} \lesssim 250M_{\odot}$ can enrich the intergalactic medium through supernova explosions (e.g., Heger et al. 2000). Roughly speaking, the former star ejects about 10% of its total mass ($\sim 1M_{\odot}$) as heavy elements through a supernova, while the latter ejects about 50% ($\sim 75M_{\odot}$).

Then, the metallicity produced by Population III stars can be estimated from the IMF (eq.[16]) as functions of ϵ , κ , α , and β . When the power indexes are tentatively assumed to be equal to each other ($\alpha = \beta$), the metallicity is evaluated as

$$Z \sim \left[3.9 \times 10^{-3} Z_{\odot} \left(\frac{\kappa}{0.5} \right) + 2.2 \times 10^{-2} Z_{\odot} \left(\frac{1 - \kappa}{0.5} \right) \right] \left(\frac{\epsilon}{10^{-2}} \right) \quad \text{for } \alpha = \beta = 1.35, \quad (21)$$

$$Z \sim \left[3.3 \times 10^{-4} Z_{\odot} \left(\frac{\kappa}{0.5} \right) + 9.3 \times 10^{-3} Z_{\odot} \left(\frac{1 - \kappa}{0.5} \right) \right] \left(\frac{\epsilon}{10^{-2}} \right) \quad \text{for } \alpha = \beta = 3, \quad (22)$$

where we took the second peak of $m_{p2} = 50M_{\odot}$. When the contribution from the high-mass component is more

significant, the metallicity is larger. If the star formation efficiency is as high as the present-day value of $\epsilon \sim 10^{-2}$ and the power indexes are around $\alpha = \beta \sim 1.35 - 3$, then the metallicity is estimated as $10^{-3} - 10^{-2} Z_{\odot}$, which is consistent with the metallicity $Z \lesssim 10^{-2} Z_{\odot}$ observed in Ly α forest clouds with $N_{\text{HI}} > 3 \times 10^{14} \text{ cm}^{-3}$ by Cowie et al. (1995) and Cowie & Songaila (1998). Thus, the heavy elements by the first enrichment may be responsible for the metallicity in the intergalactic medium at high redshifts. This might be testable with observations of the metallicity and abundance ratios of heavy elements in those objects.

Furthermore, the first enrichment by Population III stars might play a significant role in the early evolution of galaxies or abundances of the intergalactic medium observed by X-ray (e.g., Zepf & Silk 1996; Larson 1998).

7. CONCLUSIONS

We have explored the collapse and fragmentation of filamentary primordial gas clouds numerically, including the nonequilibrium processes for hydrogen molecule formation. The simulations have shown that, depending upon the initial density, the evolution of the filaments can be classified into two types. If a filament has relatively low initial density such as $n_c \lesssim 10^5 \text{ cm}^{-3}$, the radial contraction is slow due to less effective H₂ cooling, and it appreciably decelerates at density higher than a critical density, where LTE populations are achieved for the rotational levels of H₂ molecules and the cooling timescale becomes accordingly longer than the free-fall timescale. This filament tends to fragment into dense clumps before the central density reaches 10^{8-9} cm^{-3} where H₂ cooling by three-body reaction is effective, and the clump mass is more massive than some tens M_{\odot} . In contrast, if a filament is initially as dense as $n_c \gtrsim 10^5 \text{ cm}^{-3}$, more effective H₂ cooling with the help of three-body reaction allows the filament to contract up to $n \sim 10^{12} \text{ cm}^{-3}$, for which the filament becomes optically thick to H₂ lines and then the radial contraction almost stops. At this final hydrostatic stage, the clump mass is lowered down to $\approx 1 - 2M_{\odot}$ because of the high density of the filament. The dependence of clump mass upon the initial density could be translated into the dependence of the local amplitude of random Gaussian density fields or the epoch of collapse of a parent cloud. Hence, the distribution of the clump mass predicts that the initial mass function of Population III stars is likely to be bimodal with peaks of $\approx 1 - 2M_{\odot}$ and $\approx 10^2 M_{\odot}$, where the relative heights could be a function of the collapse epoch. At higher redshifts or for higher σ density fluctuations, the contribution of the lower-mass component is likely to be more significant in the IMF and the relative height of the first peak probably decreases with time because the initial densities of the filaments are likely to descend with time.

In our model, we do not take the effects of external radiation into account. As suggested by Abel et al. (2000), a single star may form at the central high-density region of the first collapsed low-mass objects. The radiative feedback from the very first stars might be significant for subsequent star formation in the surrounding medium (e.g., Ferrara 1998; Ciardi, Ferrara, & Abel 2000).

We modeled the Population III IMF as a superposition of two power-law distributions with different peaks and es-

timated the metallicity produced by Population III stars in the first collapsed objects at high redshifts. If the star formation efficiency is of the same order as the present-day value $\epsilon \sim 10^{-2}$, then the metallicity is estimated as $10^{-3} - 10^{-2} Z_\odot$. This metallicity is consistent with that observed in the intergalactic medium at high redshifts.

If a significant amount of stars with masses between a few M_\odot and $8M_\odot$ were formed, they might have evolved into white dwarfs until the present epoch. The old white dwarfs might presently reside in the galactic halo and may be related to dark component observed in microlensing experiments, i.e., massive compact halo objects (MACHOs). If the star formation efficiency is of the same order as the present-day value, then the ancient white dwarfs are likely to contribute a few tens % of the dark mass in the galactic halo, which seems to be consistent with some constraints

discussed by several authors (e.g., Charlot & Silk 1995; Alcock et al. 2000; Lasserre et al. 2000; Méndez & Minniti 2000; Hodgkin et al. 2000; Ibata et al. 2000).

We are grateful to T. Nakamoto, R. Nishi, K. Omukai, H. Susa, K. Tomisaka, and H. Uehara for valuable discussions. Numerical computations were carried out on VPP300/16R and VX/4R at the Astronomical Data Analysis Center of the National Astronomical Observatory, Japan and workstations at the Center for Computational Physics, University of Tsukuba. This work was financially supported in part by the Grant-in-Aid for Scientific Research on Priority Areas of the Ministry of Education, Science, Sports and Culture [10147205 and 11134203 (FN) and 11640225 (MU)].

APPENDIX

FORMATION OF FILAMENTARY PRIMORDIAL CLOUDS

In this appendix, we consider the formation process of filamentary primordial clouds to estimate the typical values as the initial conditions.

We premise a gravitational instability scenario for the formation of cosmic structure. A cosmological density perturbation larger than the Jeans scale at the recombination epoch forms a flat pancake-like disk. This process has been extensively studied by many authors (e.g., Zel'dovich 1970; Sunyaev & Zel'dovich 1972; Cen & Ostriker 1992a, 1992b; Umemura 1993). Although the pancake formation was originally studied by Zel'dovich (1970) in the context of the adiabatic fluctuations in baryon or hot-dark-matter-dominated universes, recent numerical simulations have shown that such pancake structures also emerge in CDM cosmology (e.g., Cen et al. 1994). Thus, the pancakes are thought to be a ubiquitous feature in gravitational instability scenarios. In the following, we reconsider the pancaking of a cosmological density perturbation and fragmentation of the pancake into filamentary clouds.

We first suppose a spherical top-hat overdense region in the Einstein-de Sitter Universe. The overdense region collapses due to self-gravity until a shock develops. After thermalization by the shock, the region forms a virialized system. The virial radius and temperature of the overdense region are then estimated as (e.g., Padmanabhan 1993)

$$r_{\text{vir}} = 1.9 \times 10^2 \text{ pc} \left(\frac{1 + z_{\text{vir}}}{30} \right)^{-1} \left(\frac{M_b}{10^6 M_\odot} \right)^{1/3} \left(\frac{\Omega_b}{0.1} \right)^{-1/3} h_{0.5}^{-2/3}, \quad (\text{A1})$$

and

$$T_{\text{vir}} = 1.2 \times 10^4 \text{ K} \left(\frac{1 + z_{\text{vir}}}{30} \right) \left(\frac{M_b}{10^6 M_\odot} \right)^{2/3} \left(\frac{\Omega_b}{0.1} \right)^{-2/3} h_{0.5}^{2/3}, \quad (\text{A2})$$

where $h_{0.5}$ is the Hubble constant in units of $50 \text{ km s}^{-1} \text{ Mpc}^{-1}$, z_{vir} is the redshift epoch of virialization, M_b is the baryonic mass, and Ω_b is the baryonic density parameter.

In a realistic situation, however, the overdense region is more or less aspherical. The deviation from spherical symmetry grows with time and a pancake disk consequently forms. After the shock is thermalized, the pressure force nearly balances the gravitational force in the vertical direction in the disk. If the radiative cooling is effective, the temperature can descend to a lower value than the virial temperature. Recent numerical simulations (e.g., Haiman et al. 1996; Abel et al. 1998; Bromm et al. 1999) have shown that when the first collapsed objects with masses of $10^{5-8} M_\odot$ are virialized, H_2 relative abundance rises from its initial value of 10^{-6} to $x_{\text{H}_2} \sim 10^{-3} - 10^{-4}$ and H_2 molecules then cool the gas to a temperature of $T \sim 300 - 500 \text{ K}$. Consequently a thin baryonic disk forms, where the baryon density overwhelms that of the extended virialized dark halo (e.g. Umemura 1993). Then we have a relation such as $2\pi G \rho_d H_d^2 \simeq c_s^2$, where ρ_d , H_d , and c_s denote the characteristic density, thickness of the disk, and sound speed, respectively. The density of the cooled disk is then estimated as

$$n = \frac{\rho_d}{\mu} = \frac{G}{2\pi k T} \frac{M_b^2}{R_d^4} \quad (\text{A3})$$

$$= 5.1 \times 10^4 \text{ cm}^{-3} \left(\frac{\alpha}{0.1} \right)^{-4} \left(\frac{1 + z_{\text{vir}}}{30} \right)^4 \left(\frac{T}{500 \text{ K}} \right)^{-1} \left(\frac{M_b}{10^6 M_\odot} \right)^{2/3} \left(\frac{\Omega_b}{0.1} \right)^{4/3} h_{0.5}^{-8/3}, \quad (\text{A4})$$

where μ is the mean molecular weight, R_d is the disk radius, and $\alpha (\equiv R_d/r_{\text{vir}})$ is the disk radius in units of r_{vir} . Furthermore, an overdense region acquires angular momentum through tidal spin-up by their surrounding fluctuations.

Then the overdense region cannot collapse into a disk smaller than the centrifugal barrier. The radius of the centrifugal barrier is given by

$$r_{\text{barr}} \simeq 0.01 r_{\text{vir}} \left(\frac{\Omega_b}{0.1} \right)^{-1} \left(\frac{\lambda}{0.05} \right)^2 \quad (\text{A5})$$

where λ is a dimensionless spin parameter $\lambda \equiv J|E|^{1/2}G^{-1}M^{-5/2}$ (Sasaki & Umemura 1996), which is peaked around $\lambda = 0.05$ (Heavens & Peacock 1988). The symbols J and E denote the total angular momentum and energy, respectively. The radius r_{barr} gives a lower bound for the size of the first collapsed pancake, which leads to a condition as $\alpha \gtrsim 0.01$.

According to the linear theory of the disk in hydrostatic equilibrium, the disk is most unstable to the perturbation with the wavelength of $\lambda_{\text{max}} = 4\pi H_d$ (e.g., Larson 1985). When the most unstable perturbation grows in the disk, the disk fragments into filamentary clouds rather than spherical clouds. Then, the separation of the filaments is equal to λ_{max} .

If all the mass within one wavelength λ_{max} collapses into one filament of line mass l , then the mass of the filament is given as

$$M_{\text{fil}} \sim l R_d = 8.3 \times 10^4 M_{\odot} \left(\frac{\alpha}{0.1} \right) \left(\frac{1+z_{\text{vir}}}{30} \right)^{-1} \left(\frac{T}{500\text{K}} \right) \left(\frac{M_b}{10^6 M_{\odot}} \right)^{1/3} \left(\frac{\Omega_b}{0.1} \right)^{-1/3} h_{0.5}^{-2/3} . \quad (\text{A6})$$

The number of filaments formed from the parent disk is then estimated as

$$N_{\text{fil}} = \frac{M_b}{M_{\text{fil}}} \simeq 12 \left(\frac{\alpha}{0.1} \right)^{-1} \left(\frac{1+z_{\text{vir}}}{30} \right) \left(\frac{T}{500\text{K}} \right)^{-1} \left(\frac{M_b}{10^6 M_{\odot}} \right)^{2/3} \left(\frac{\Omega_b}{0.1} \right)^{1/3} h_{0.5}^{2/3} . \quad (\text{A7})$$

REFERENCES

Abel, T., Anninos, P. A., Norman, M. L., & Zhang, Y. 1998, ApJ, 508, 518
 Abel, T., Norman, M. L., & Bryan, G. L. ApJ, in press
 Alcock, C. et al. 2000, submitted to ApJ(astro-ph/0001272)
 Audouze, J., & Silk, J. 1995, ApJ, 451, L49
 Bond, J. R., Carr, B. J., & Arnett, W. D. 1984, ApJ, 280, 825
 Bromm, V., Coppi, P. S., Larson, R. B. 1999, ApJ, 527, L5
 Carr, B. J., Bond, J. R., & Arnett, W. D. 1984, ApJ, 277, 445
 Carr, B. J. 1994, ARA&A, 32, 531
 Carlberg, R. G. 1981, MNRAS, 197, 1021
 Carlot, S., Silk, J. 1995, ApJ, 445, 124
 Castor, J. I. 1970, MNRAS, 149, 111
 Ciardi, B., Ferrara, A., & Abel, T. 2000, ApJ, 533, 594
 Cen, R. 1992, ApJ, 78, 341
 Cen, R., & Ostriker, J. P. 1992a, ApJ, 393, 22
 Cen, R., & Ostriker, J. P. 1992b, ApJ, 399, 331
 Ciardi, B., Ferrara, A., & Abel, T. 2000, ApJ, 533, 594
 Chiosi, C. 2000, in The First Stars, eds. A. Weiss, T. Abel, & V. Hill, Springer, p.95
 Couchman, H. M. P., & Rees, M. J. 1986, MNRAS, 221, 53
 Cowie, L. L., Songaila, A., Kim, T.-S., & Hu, E. M. 1995, AJ, 109, 1522
 Cowie, L. L., & Songaila, A. 1998, Nature, 394, 44
 Ferrara, A. 1998, ApJ, 499, L17
 Fukugita, M., & Kawasaki, M. 1994, MNRAS, 269, 563
 Galli, D., & Palla, F. 1998, A&A, 335, 403
 Gnedin, N. Y. 2000, ApJ, in press (astro-ph/9909383)
 Gnedin, N. Y., & Ostriker, J. P. 1997, ApJ, 486, 581
 Goldreich, P. & Kwan, J. 1974, ApJ, 189, 441
 Haiman, Z., & Loeb, A. 1997, ApJ, 483, 21
 Haiman, Z., & Loeb, A. 1998, ApJ, 503, 505
 Haiman, Z., Rees, M. J., & Loeb, A. 1996, ApJ, 467, 522
 Haiman, Z., Rees, M. J., & Loeb, A. 1997, ApJ, 476, 458
 Haiman, Z., Thoul, A. A., & Loeb, A. 1996, ApJ, 464, 523
 Heavens, A., & Peacock, J. 1988, MNRAS, 232, 339
 Heger, A., Woosley, S. E., & Waters, R. 2000, in The First Stars, eds. A. Weiss, T. Abel, & V. Hill, Springer, p.121
 Ibata, R., Urwin, M., Bienaym, O., Scholz, R. & Guibert, J. 2000, ApJ, 532, L41
 Hodgkin, S. T., Oppenheimer, B. R., Hambly, N. C., Jameson, R. F., Smartt, S. J., & Steele, I. A. 2000, Nature, 403, 54
 Hollenbach, D., & McKee, C. F. 1979, ApJS, 342, 306
 Hutchins, J. B., 1976, ApJ, 205, 103
 Larson, R. B. 1985, MNRAS, 214, 379
 Larson, R. B. 1998, MNRAS, 301, 569
 Larson, R. B., 2000, in Star Formation From the Small to the Large Scale, F. Favata, A. A. Kaas, & A. Wilson (eds.), in press
 Lasserre, T. et al. 2000, submitted to A&A(astro-ph/0002253)
 Lepp, S., & Shull, M. 1984, ApJ, 280, 465
 Matsuda, T., Sato, H., & Takeda, H. 1969, Prog. Theor. Phys., 42, 219
 McWilliam, A., Preston, G. W., Sneden, C., & Searle, L. 1995, AJ, 109, 2757
 Méndez, R. A., & Minniti, D. 2000, ApJ, 529, 911
 Miralda-Escudé J., & Rees M. J., 1998, ApJ, 497, 21
 Nakamura, F., Hanawa, T., & Nakano, T. 1993, PASJ, 45, 551
 Nakamura, F., & Umemura, M. 1999, ApJ, 515, 239 (Paper I)
 Nishi, R., Susa, H., Uehara, H., Yamada, M., & Omukai, K. 1998, Prog. Theor. Phys., 100, 881
 Nobuta, K., & Hanawa, T. 1999, ApJ, 510, 614
 Omukai, K., & Nishi, R., 1998, ApJ, 508, 141
 Omukai, K., Nishi, R., Uehara, H., & Susa, H. 1998, Prog. Theor. Phys., 99, 747
 Ostriker, J. P., & Gnedin, N. Y. 1996, ApJ, 472, L63
 Padmanabhan, T. 1993, Structure Formation in the Universe (Cambridge University Press)
 Palla, F., Salpeter, E. E., & Stahler, S. W., 1983, ApJ, 271, 632
 Portinari, L., Chiosi, C., & Bressan, A. 1998, A&A, 334, 505
 Rees, M. J. 1999, preprint (astro-ph/9912345)
 Ryan, S. G., Norris, J. E., & Beers, T. C. 1996, ApJ, 471, 254
 Sasaki, S., & Umemura, M. 1996, ApJ, 462, 104
 Shapiro, P. R., & Kang, H. 1987, ApJ, 318, 32
 Silk, J. 1977, ApJ, 214, 152
 Silk, J. 1983, MNRAS, 205, 705
 Shigeyama, T., & Tsujimoto, T. 1998, ApJ, 507, L135
 Songaila, A., & Cowie, L. L. 1996, AJ, 112, 335
 Stodolkiewicz, J.S. 1963, Acta Astron., 13, 30
 Sunyaev, R. A., & Zel'dovich, Ya. B. 1972, A&A, 20, 189
 Susa, H., Uehara, H., & Nishi, R. 1996, Prog. Theor. Phys., 96, 1073
 Susa, H., Uehara, H., Nishi, R., & Yamada, M. 1998, Prog. Theor. Phys., 100, 63
 Tegmark, M., & Silk, J. 1994, ApJ, 441, 458
 Tegmark, M., Silk, J., & Blanchard, A. 1994, ApJ, 420, 484
 Tegmark, M., Silk, J., Rees, M., Blanchard, A., Abel, T., & Palla, F. 1997, ApJ, 474, 1
 Tsuribe, T. 2000, in The First Stars, A. Weiss, T. Abel, & V. Hill (eds.), p.277, Springer, p. 273
 Yoneyama, T. 1972, PASJ, 24, 87
 Yoshiii, Y., & Saio 1986, ApJ, 301, 587
 Uehara, H., Susa, H., Nishi, R., & Yamada, M. 1996, ApJ, 473, L95
 Umemura, M., Loeb, A., & Turner, E. 1993, ApJ, 419, 459
 Umemura, M. 1993, ApJ, 406, 361
 Valageas, P., & Silk, J. 1999, A&A, 347, 1
 Verner, D. A., & Ferland, G. J. 1996, ApJS, 103, 467
 Zel'dovich, Ya. B. 1970, A&A, 5, 84
 Zepf, S. E., & Silk, J. 1996, ApJ, 466, 114

TABLE 1
REACTION RATE COEFFICIENTS

Reactions		Rate Coefficients ^a	Reference
(H1)	$H + e \rightarrow H^+ + 2e$	$k_{H1} = 5.85 \times 10^{-11} T^{0.5} \exp(-157809.1/T) [1 + (T/10^5)^{0.7}]^{-1}$	C92
(H2)	$H^+ + e \rightarrow H + h\nu$	$k_{H2} = 8.40 \times 10^{-11} T^{-1/2} (T/10^3)^{-0.2} [1 + (T/10^6)^{0.7}]^{-1}$	C92
(H3)	$H + H \rightarrow H + H^+ + e$	$k_{H3} = 1.7 \times 10^{-4} k_1$	PSS83
(H4)	$H + e \rightarrow H^- + h\nu$	$k_{H4} = 1.4 \times 10^{-18} T^{0.928} \exp(-T/16200)$	GP98
(H5)	$H + H^- \rightarrow H_2 + e$	$k_{H5} = \begin{cases} 1.5 \times 10^{-9} & T \leq 300\text{K} \\ 4.0 \times 10^{-9} T^{-0.17} & T > 300\text{K} \end{cases}$	GP98
(H6)	$H + H^+ \rightarrow H_2^+ + h\nu$	$k_{H6} = \text{dex}[-19.38 - 1.523 \log T + 1.118(\log T)^2 - 0.1269(\log T)^3]$	GP98
(H7)	$H_2^+ + H \rightarrow H_2 + H^+$	$k_{H7} = 6.4 \times 10^{-10}$	GP98
(H8)	$H_2 + H \rightarrow 3H$	k_{H8} [see eqs. (B6)–(B8) in reference]	SK87
(H9)	$H_2 + H^+ \rightarrow H_2^+ + H$	$k_{H9} = \begin{cases} 3.0 \times 10^{-10} \exp(-21050/T) & T \leq 10^4\text{K} \\ 1.5 \times 10^{-10} \exp(-14000/T) & T > 10^4\text{K} \end{cases}$	GP98
(H10)	$H_2 + e \rightarrow H + H^-$	$k_{H10} = 2.7 \times 10^{-8} T^{-1.27} \exp(-43000/T)$	GP98
(H11)	$H_2 + e \rightarrow 2H + e$	$k_{H11} = 4.38 \times 10^{-10} T^{0.35} \exp(-102000/T)$	SK87
(H12)	$H_2 + H_2 \rightarrow 2H + H_2$	k_{H12} [see eqs. (B6)–(B8) in reference]	SK87
(H13)	$H^- + e \rightarrow H + 2e$	$k_{H13} = 4.0 \times 10^{-12} \exp(-43000/T)$	SK87
(H14)	$H^- + H \rightarrow 2H + e$	$k_{H14} = 5.3 \times 10^{-20} T^{2.17} \exp(-8750/T) + 5.7 \times 10^{-6} T^{-0.5} + 6.3 \times 10^{-8}$	SK87
(H15)	$H^- + H^+ \rightarrow 2H$	$k_{H15} = -9.2 \times 10^{-11} T^{0.5} + 4.4 \times 10^{-13} T$	GP98
(H16)	$H^- + H^+ \rightarrow H_2^+ + e$	$k_{H16} = \begin{cases} 6.9 \times 10^{-9} T^{-0.35} & T \leq 8000\text{K} \\ 9.6 \times 10^{-7} T^{-0.9} & T > 8000\text{K} \end{cases}$	GP98
(H17)	$H_2^+ + e \rightarrow 2H$	$k_{H17} = 2.0 \times 10^{-7} T^{-0.5}$	GP98
(H18)	$H_2^+ + H^- \rightarrow H + H_2$	$k_{H18} = 5.0 \times 10^{-6} T^{-0.5}$	SK87
(H19)	$3H \rightarrow H_2 + H$	$k_{H19} = 5.5 \times 10^{-29} T^{-1}$	PSS83
(H20)	$2H + H_2 \rightarrow 2H_2$	$k_{H20} = k_{H19}/8$	PSS83
(He1)	$He + e \rightarrow He^+ + 2e$	$k_{He1} = 2.38 \times 10^{-11} T^{-0.5} \exp(-285335.4/T) [1 + (T/10^5)^{0.5}]^{-1}$	C92
(He2)	$He^+ + e \rightarrow He^{++} + 2e$	$k_{He2} = 5.68 \times 10^{-12} T^{0.5} \exp(-631515.0/T) [1 + (T/10^5)^{0.5}]^{-1}$	C92
(He3)	$He^+ + e \rightarrow He + h\nu$	$k_{He3} = 3.294 \times 10^{-11} \left[\sqrt{\frac{T}{15.54}} \left(1 + \sqrt{\frac{T}{15.54}} \right)^{0.309} \times \left(1 + \sqrt{\frac{T}{3.676 \times 10^7}} \right)^{1.691} \right]^{-1}$	VF96
(He4)	$He^{++} + e \rightarrow He^+ + h\nu$	$k_{He4} = 1.891 \times 10^{-10} \left[\sqrt{\frac{T}{9.37}} \left(1 + \sqrt{\frac{T}{9.37}} \right)^{0.2476} \times \left(1 + \sqrt{\frac{T}{2.774 \times 10^6}} \right)^{1.7524} \right]^{-1}$	VF96
(He5)	$He + H^+ \rightarrow He^+ + H$	$k_{He5} = 4.0 \times 10^{-37} T^{4.74}$	GP98
(He6)	$He^+ + H \rightarrow He + H^+$	$k_{He6} = 3.7 \times 10^{-25} T^{2.06} \left[1 + 9.9 \exp\left(-\frac{T}{2570}\right) \right]$	GP98

^aThe units of rate coefficients are taken to be $\text{cm}^3 \text{ s}^{-1}$ for two-body reactions and $\text{cm}^6 \text{ s}^{-1}$ for three-body reactions.

NOTE.— C92: Cen (1992); PSS83: Palla et al. (1983); GP98: Galli & Palla (1998); SK87: Shapiro & Kang (1987); VF96: Verner & Ferland (1996)

TABLE 2
MODEL PARAMETERS

Model	f	n_c (cm $^{-3}$)	T (K)	x_{H_2}
A1a	1.5	10	400	10^{-4}
A1b	1.5	10	300	10^{-3}
A2a	1.5	10^2	400	10^{-4}
A2b	1.5	10^2	300	10^{-3}
A3a	1.5	10^3	400	10^{-4}
A3b	1.5	10^3	300	10^{-3}
A4a	1.5	10^4	400	10^{-4}
A4b	1.5	10^4	300	10^{-3}
A5a	1.5	10^5	400	10^{-4}
A5b	1.5	10^5	300	10^{-3}
A6a	1.5	10^6	400	10^{-4}
A6b	1.5	10^6	300	10^{-3}
B1a	2	10	400	10^{-4}
B1b	2	10	300	10^{-3}
B2a	2	10^2	400	10^{-4}
B2b	2	10^2	300	10^{-3}
B3a	2	10^3	400	10^{-4}
B3b	2	10^3	300	10^{-3}
B4a	2	10^4	400	10^{-4}
B4b	2	10^4	300	10^{-3}
B5a	2	10^5	400	10^{-4}
B5b	2	10^5	300	10^{-3}
B6a	2	10^6	400	10^{-4}
B6b	2	10^6	300	10^{-3}
C1a	4	10	400	10^{-4}
C1b	4	10	300	10^{-3}
C2a	4	10^2	400	10^{-4}
C2b	4	10^2	300	10^{-3}
C3a	4	10^3	400	10^{-4}
C3b	4	10^3	300	10^{-3}
C4a	4	10^4	400	10^{-4}
C4b	4	10^4	300	10^{-3}
C5a	4	10^5	400	10^{-4}
C5b	4	10^5	300	10^{-3}
C6a	4	10^6	400	10^{-4}
C6b	4	10^6	300	10^{-3}

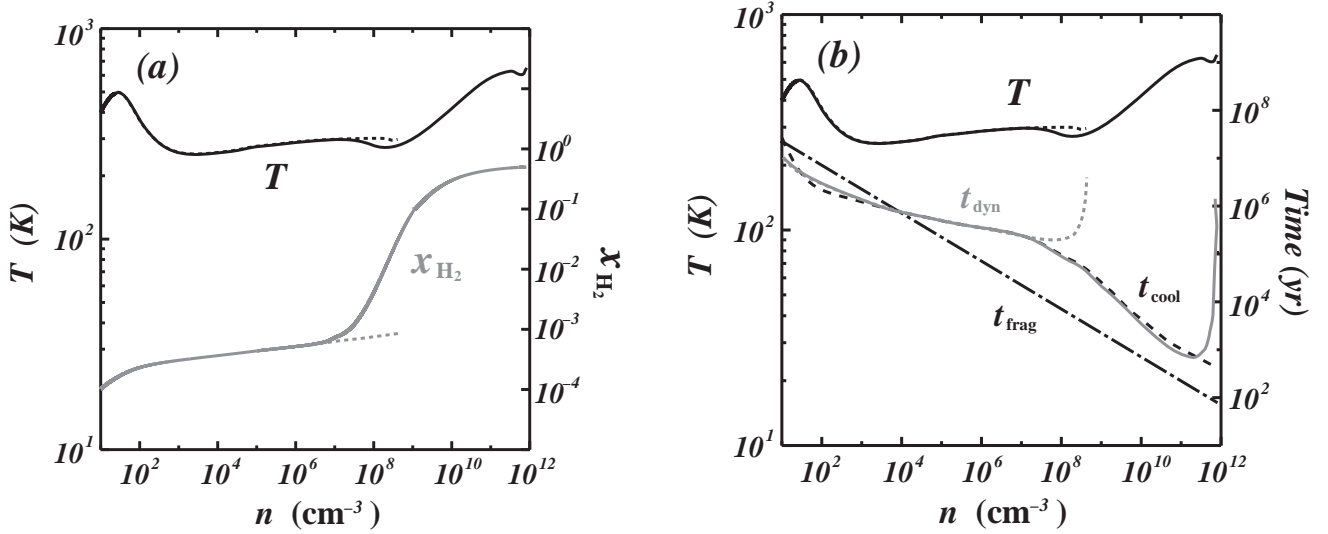


FIG. 1.— (a) Evolution of the temperature (T_c) and the H_2 relative abundance ($x_{H_2,c}$) at the center for model A1a with no density fluctuations. The model has the initial parameters of $(n_0, T_0, f) = (10 \text{ cm}^{-3}, 400 \text{ K}, 1.5)$. For comparison, we also show the evolutional paths of the model in which the three-body reactions are neglected (dotted lines). The temperature stays nearly constant at 300 – 500 K over the seventh order of magnitude in density. When the central density reaches $n_c \sim 10^8 \text{ cm}^{-3}$, the three-body reactions of H_2 formation become dominant and almost all the hydrogen atoms become into H_2 molecules. Thus, the H_2 abundance steeply rises around $n_c \sim 10^8 \text{ cm}^{-3}$. When the density reaches $n_c \sim 10^{12} \text{ cm}^{-3}$, the cloud becomes optically thick to the H_2 lines. (b) Evolution of the contraction time (solid line), the cooling time (dashed line), and the fragmentation time (dashed-dotted line). For comparison, we also showed the evolution of the contraction time for the model in which the three-body reactions are neglected (dotted lines). The contraction becomes slower after the central density reaches the critical density of H_2 ($n_{\text{cr}} \sim 10^3 \text{ cm}^{-3}$). When the density reaches $n_c \sim 10^{12} \text{ cm}^{-3}$, the cloud becomes optically thick to the H_2 lines, and the contraction essentially stops at that stage. For the model without the three-body reactions, the contraction decelerates at the stage at which $n_c \sim 10^9 \text{ cm}^{-3}$ because of less effective H_2 cooling.

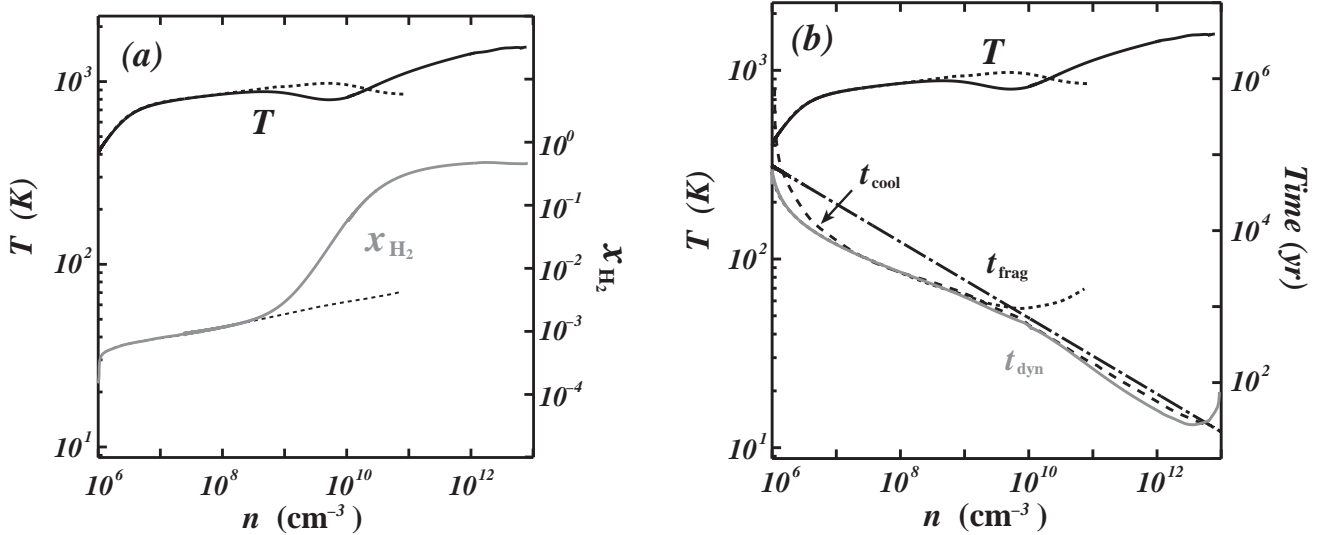


FIG. 2.— Same as Figure 1 but for model C6a. The model has the initial parameters of $(n_0, T_0, f) = (10^6 \text{ cm}^{-3}, 400 \text{ K}, 4)$. The overall evolution is qualitatively similar to that of model A1a. In this model, the contraction time does not exceed the fragmentation time until the cloud becomes optically thick to the H_2 lines and the contraction essentially stops.

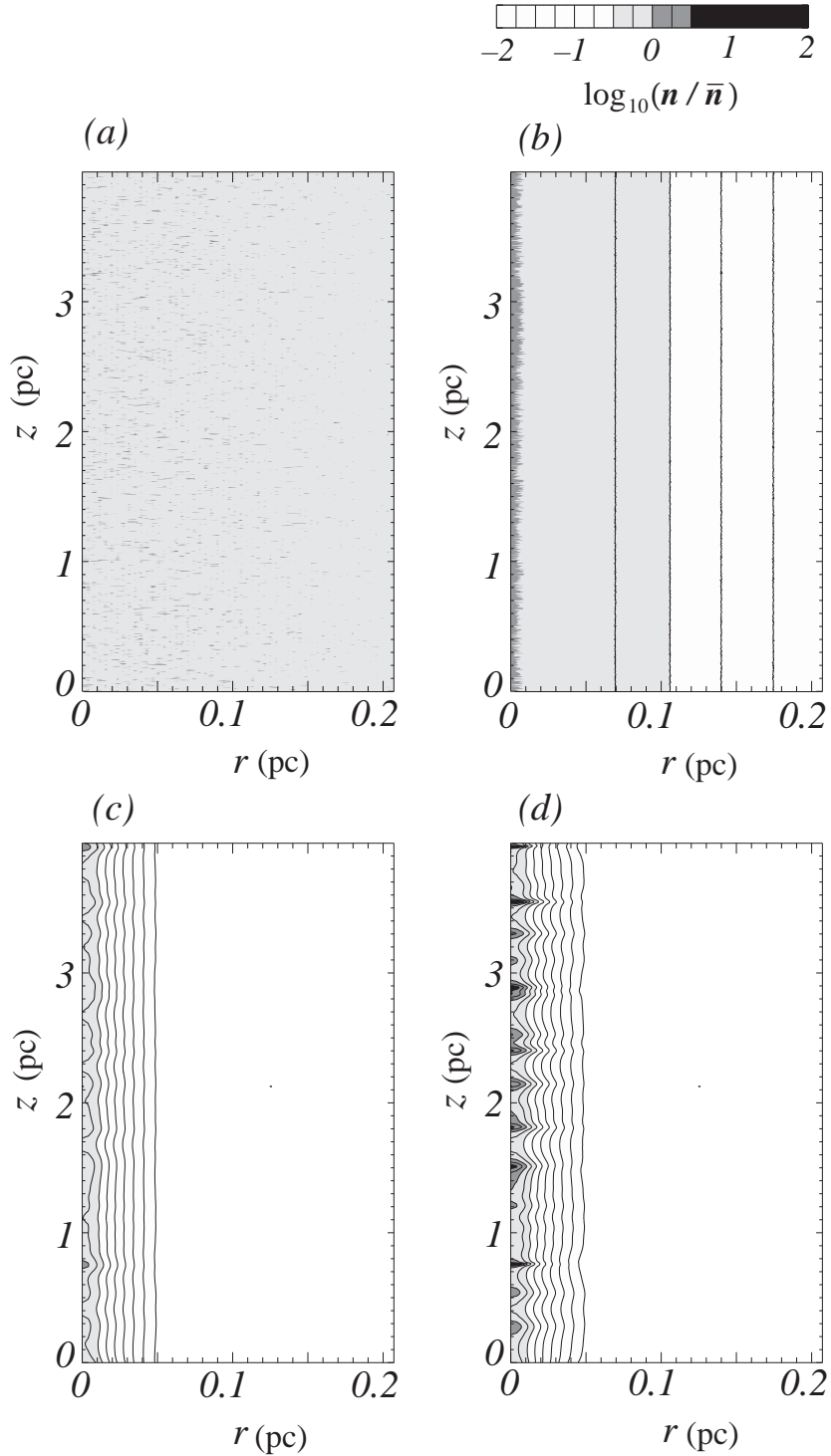


FIG. 3.— Density and velocity distributions in the $r - z$ plane for model A4a at four different stages: (a) $t = 0$ ($\bar{n}_c = 1.0 \times 10^4 \text{ cm}^{-3}$, initial state), (b) $t = 5.9 \times 10^5 \text{ yr}$ ($\bar{n}_c = 9.9 \times 10^5 \text{ cm}^{-3}$), (c) $t = 8.1 \times 10^5 \text{ yr}$ ($\bar{n}_c = 5.1 \times 10^7 \text{ cm}^{-3}$), and (d) $t = 8.2 \times 10^5 \text{ yr}$ ($\bar{n}_c = 7.5 \times 10^7 \text{ cm}^{-3}$). At the initial state, scale-invariant density fluctuations with an amplitude of $\delta = 0.1$ are added. When the density reaches 10^7 cm^{-3} , unstable density fluctuations begin to grow nonlinearly because the contraction time becomes longer than the fragmentation time. The mean mass and separation of the clumps are estimated as $\sim 250M_\odot$ and 0.24 pc at the final stage of the computation, respectively.

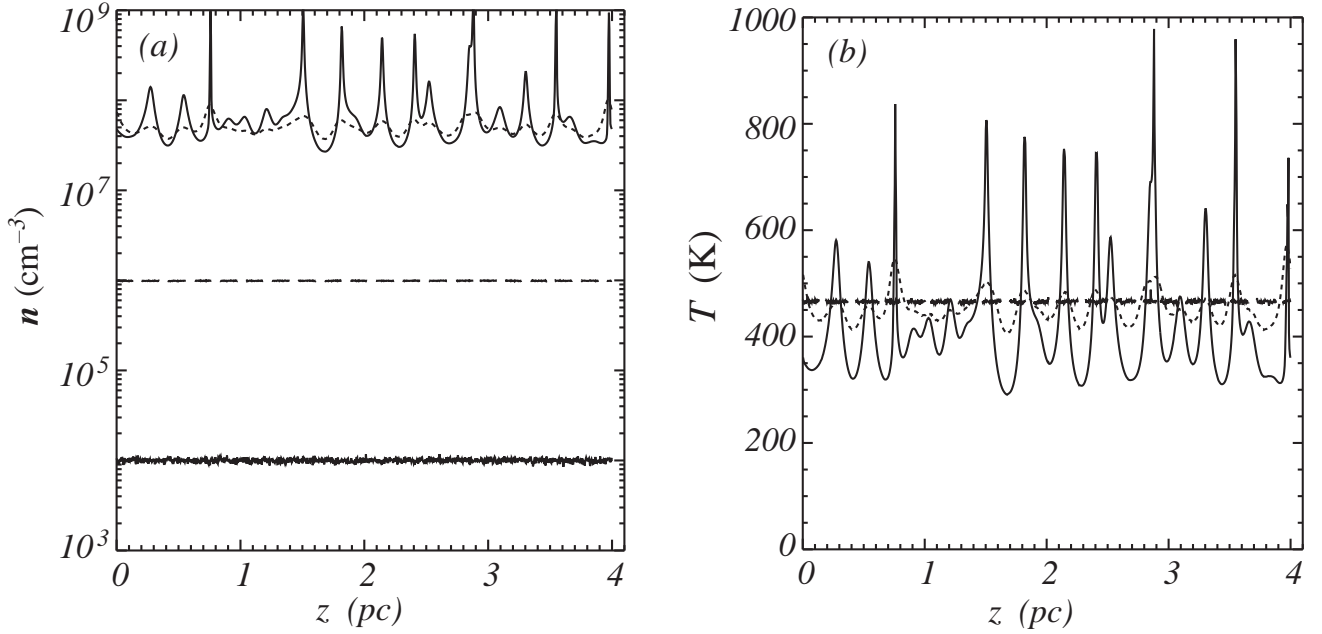


FIG. 4.— Evolution of (a) the density and (b) velocity distributions in the z -axis for model A4a with scale-invariant density fluctuations of $\delta = 0.1$. They are depicted at the stages at which $t = 0$ (solid lines), $t = 5.9 \times 10^5$ yr (long dashed lines), $t = 8.1 \times 10^5$ yr (short dashed lines), and $t = 8.2 \times 10^5$ yr (solid lines). When the density reaches 10^7 cm^{-3} , the density fluctuations begin to grow nonlinearly, and dense clumps form. In the clumps, the contraction is accelerated, and the temperature accordingly rises.

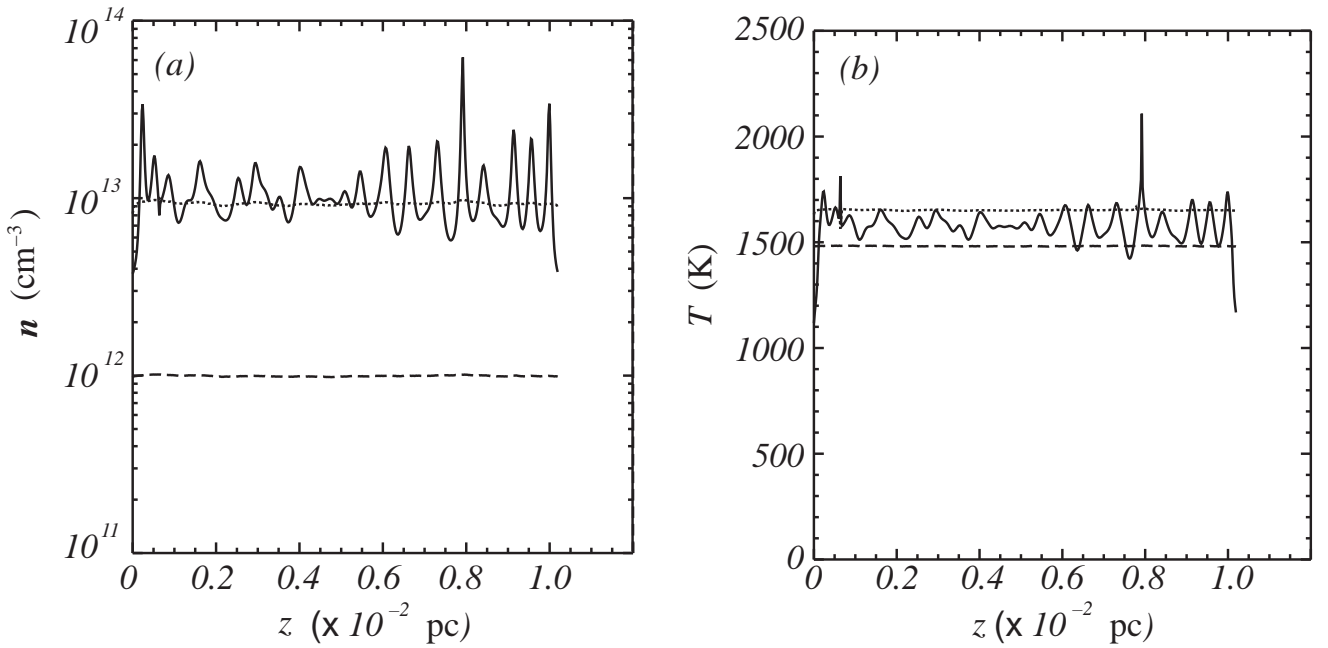


FIG. 5.— Evolution of (a) the density and (b) velocity distributions in the z -axis for model C6a with scale-invariant density fluctuations of $\delta = 0.1$. They are depicted at the stages at which $t = 5.458 \times 10^4$ yr (long dashed lines), $t = 5.464 \times 10^4$ yr (dotted lines), and $t = 5.47 \times 10^4$ yr (solid lines). When the density reaches $\sim 4 \times 10^{12} \text{ cm}^{-3}$, the radial contraction essentially stops; then, the density fluctuations begin to grow nonlinearly, and dense clumps form.

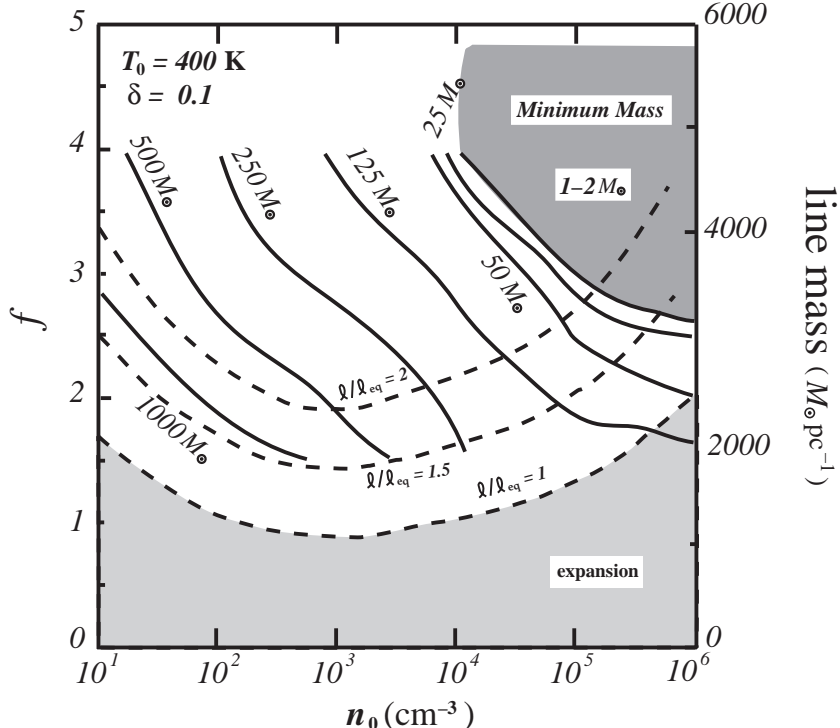


FIG. 6.— Dependence of fragment mass on the initial central density of a filament n_0 and a parameter f which corresponds to the initial line mass shown by the right ordinate. Scale-invariant ($\nu = -1$) density fluctuations with an amplitude of $\delta = 0.1$ are assumed. Solid lines denote the contour lines of the averaged fragment mass. Dashed lines show the line masses of the filaments formed by cosmological collapse and fragmentation (see text and the Appendix). The numbers attached to the dashed lines denote the line masses normalized with the equilibrium value (e.g., $l/l_{\text{eq}} = 1$, 1.5, and 2). When the line mass of the filament is less than $l/l_{\text{eq}} = 1$, the cloud expands because the pressure force is greater than the gravitational force (*light-gray region*). The averaged fragment mass depends on the initial parameters. For larger f and/or higher initial density, the fragment mass is lower. The maximum and minimum masses are estimated as $10^3 M_\odot$ and $1 \sim 2 M_\odot$, respectively. These two masses are related to the microphysics of H₂ molecules. The former corresponds to the Jeans mass at the stage at which the density reaches the critical density of H₂ molecules, while the latter corresponds to the Jeans mass at the stage at which the cloud becomes opaque to the H₂ lines. There is a steep boundary in the fragment mass at $n_0 \sim 10^{5-6} \text{ cm}^{-3}$ and $f \gtrsim 3$. For the models with $n_0 \gtrsim 10^5 \text{ cm}^{-3}$, the fragment masses take their minimum at $1 \sim 2 M_\odot$, while for the models with $n_0 \lesssim 10^5 \text{ cm}^{-3}$, they are greater than $\sim 10^2 M_\odot$. This sensitivity in the fragment mass comes from the rapid increase in the H₂ abundance due to the three-body reactions.

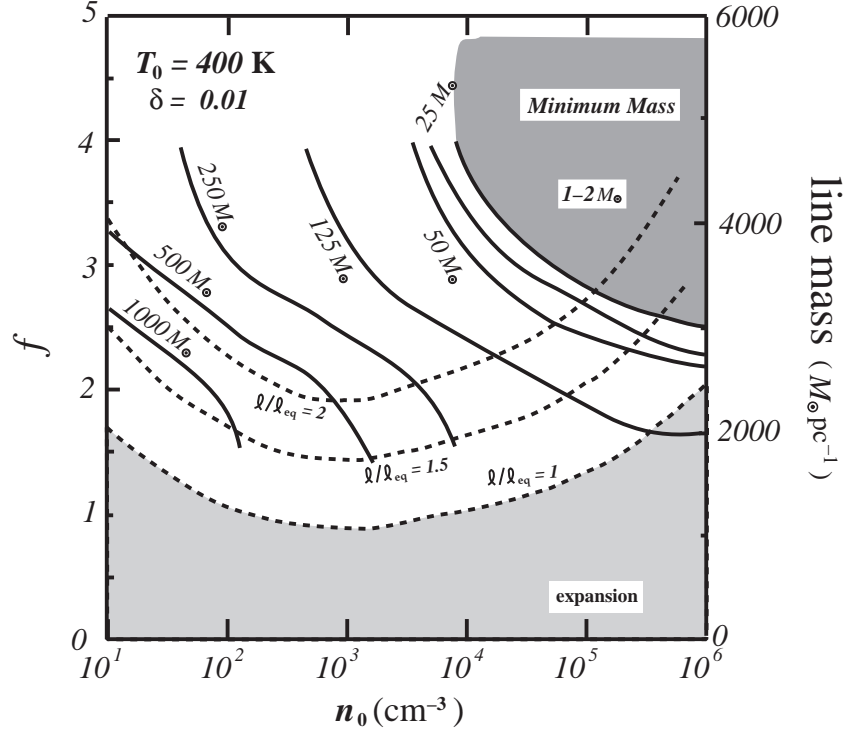


FIG. 7.— Same as Figure 6 but for $\delta = 0.01$. This figure shows that the dependence on the fluctuation amplitude is quite weak and the fragment mass is not basically altered.

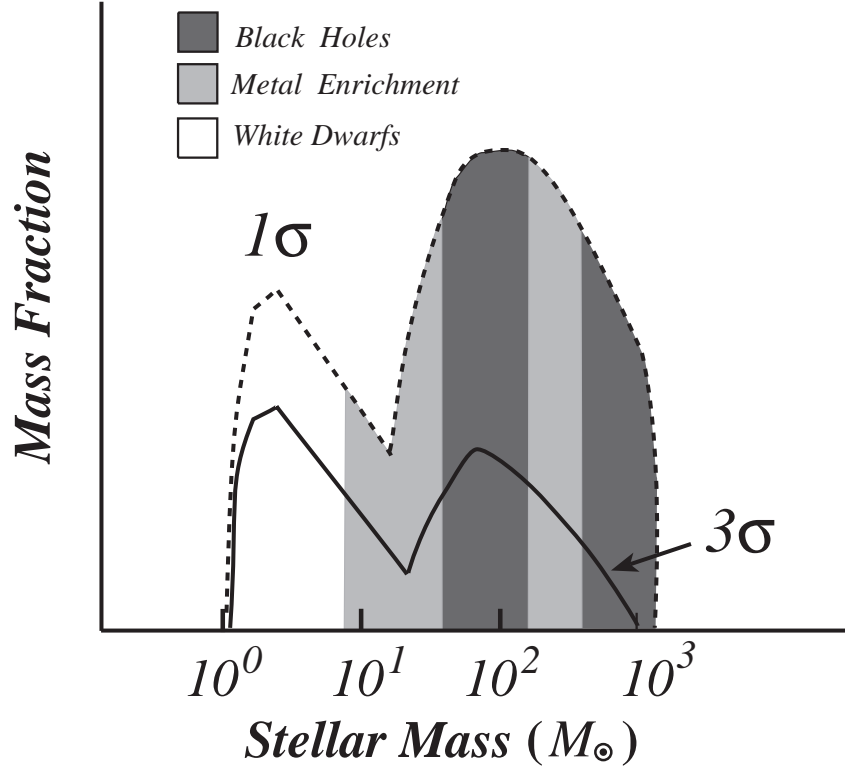


FIG. 8.— Schematic initial mass function of Population III stars. Solid and dashed lines are the IMFs for 3σ and 1σ density fluctuations, respectively. The IMF of Population III stars is likely to be bimodal and approximated by a superposition of two power-law like components with two different peaks of $m_{p1} \approx 1 - 2M_\odot$ and $m_{p2} \approx \text{a few} \times 10 - 10^2 M_\odot$. The relative height of the first peak descends with time compared to the second peak. According to a recent theory of stellar evolution, stars with masses between $1 - 2M_\odot$ and $8M_\odot$ are likely to evolve to white dwarfs that may reside in galactic halos as baryonic dark matter. Stars with masses between $8M_\odot$ and $35M_\odot$ probably evolve to supernovae and eject heavy elements in the intergalactic medium. Stars with masses between $35M_\odot$ and $10^2 M_\odot$ and greater than $250M_\odot$ are likely to collapse into black holes and may be responsible for baryonic dark matter. Stars with masses between $10^2 M_\odot$ and $250M_\odot$ probably explode as supernovae and inject heavy elements into the intergalactic medium.